Materials Science and Engineering B 288 (2023) 116195

Contents lists available at ScienceDirect

Materials Science & Engineering B

journal homepage: www.elsevier.com/locate/mseb

Type-I/Type-II Transition of $MoSe_2$/g-GaN van der Waals heterostructures mediated by biaxial strain and electric field for overall water splitting

Sajid Ur Rehman [a,b], Zeeshan Tariq [a,b], Bin Zou [a,b], Faheem K. Butt [c], Xiaoming Zhang [a,b,*], Shuai Feng [a,b], Bakhtiar Ul Haq [d,e], Chuanbo Li [a,b,*]

[a] School of Science, Minzu University of China, Beijing 100081, China
[b] Optoelectronics Research Center, Minzu University of China, Beijing 100081, People's Republic of China
[c] Department of Physics, Division of Science and Technology, University of Education Lahore, 54770, Pakistan
[d] Faculty of Science Education, Jeju National University, Jeju 63243, Republic of Korea
[e] Department of Physics, King Khalid University, Abha 62529, Saudi Arabia

ARTICLE INFO

Keywords:
2D heterostructures
Band alignment
Direct bandgap
Photocatalyst
High absorption

ABSTRACT

Nowadays, the fabrication of van der Waals heterostructures (vdWHs) from a variety of novel and existing two-dimensional materials has been regarded as an effective approach since it unravels excellent photocatalytic properties. Especially, transforming type-I to type-II vdWHs has gained significant attention due to efficient charge separation in photocatalytic, and photovoltaic devices. Here, we suggest two-dimensional $MoSe_2$/GaN vdW heterostructures along with their mechanical, electronic, photocatalytic, and optical properties using hybrid density functional. The stability of vertically stacked $MoSe_2$/GaN vdWHs is endorsed via binding energy, elastic constants, phonon dispersion, and ab-initio molecular dynamics simulation (AIMD). The HSE band structure and band alignment exhibit that $MoSe_2$/GaN vdWH has a direct bandgap and suitable band edges for the hydrogen evolution reaction (HER) ($\Delta E_c \geq 0.36$ eV) and oxygen evolution reaction (OER) ($\Delta E_v \geq 0.33$ eV). The empirical and DFT schemes reveal that the $MoSe_2$/GaN vdWHs have an intrinsic type-I band alignment with a direct bandgap and have adequately high kinetic over potentials to easily start the redox reaction. Furthermore, it's also anticipated that type-I $MoSe_2$/GaN vdWHs could be transformed to type-II vdWHs under mild strains and external electric fields, which would be favorable for effective charge separation and transportation. Notably, $MoSe_2$/GaN vdWH shows a significantly high optical absorption of nearly 10^5 cm^{-1} in the visible and ultraviolet regions which could be more easily tuned with applied strain. Current work demonstrates that the design and modulation of $MoSe_2$/GaN vdW heterostructures under strain and an electric field could open new directions for identifying promising photocatalysts in a wide solar spectrum.

1. Introduction

Energy and environmental concerns are two big barriers to human society's long-term growth. After the groundbreaking work of Fujishima and Honda in 1972 [1] on photo-electrochemical overall water splitting on a TiO_2 electrode, photocatalysis has been viewed as a suitable technique for converting solar power into ideal hydrogen (H_2) energy. Despite the fact that photocatalytic technology has gained international recognition for its safe, clean, economic and renewable characteristics. However, the photocatalytic efficiency of publicly known photocatalysts is still very far from industrial applications, particularly in solar-to-fuel conversion [2–5].

Vertical van der Waals heterostructures (vdWHs) of nanocomposites stacked by different (or sometimes the same) 2D structures, have earned growing attention due to the probability of interesting characteristics of their constituent layers [6–9]. Recently, epitaxial growth and chemical vapor deposition (CVD) approaches have been used to make a variety of vertical vdW heterostructures of nanocomposites, including MoS_2/h-BN [10], SnSe/$MoSe_2$ [11], and WS_2/MoS_2 [12]. Two-dimensional vdW heterostructure nanocomposites are currently being viewed as a viable method for developing novel optoelectronic devices with unique properties not seen in their constituent layers. Particularly, 2D vdWHs of novel nanocomposites displaying type-II band alignment with remarkable results in photocatalysis [13–16] and photovoltaic [17–19] devices

* Corresponding authors at: School of Science, Minzu University of China, Beijing 100081, China.
E-mail addresses: xmzhang@muc.edu.cn (X. Zhang), cbli@muc.edu.cn (C. Li).

https://doi.org/10.1016/j.mseb.2022.116195
Received 1 December 2021; Received in revised form 26 October 2022; Accepted 29 November 2022
Available online 13 December 2022

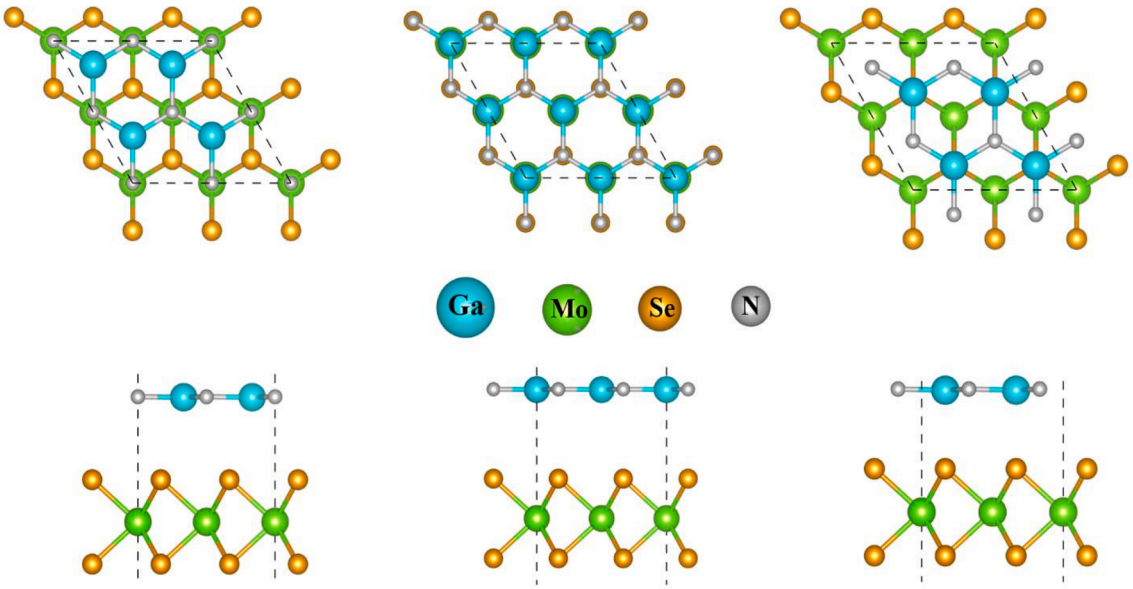

Fig. 1. Illustrated the top views and side views of three different stacked $MoSe_2$/GaN vdWHs **(a)** AA stacking, **(b)** AB stacking and **(c)** BB stacking types.

due to their intriguing optoelectronic properties.

Many graphene-like 2D compounds, such as 2D molybdenum diselenide ($MoSe_2$) [20] and gallium nitride (GaN) [21] monolayers, have been discovered and explored after Novoselov and Geim efficiently separated graphene from graphite [22]. Transition metal dichalcogenides (TMDs) monolayers, a type of 2D material, have drawn extensive attention in recent decades because of their rich physics and exciting applications in photonics and nanoelectronics [23–26]. Molybdenum diselenide ($MoSe_2$), an ultrathin monolayer of TMDs, has emerged as a potential substitute to graphene for optoelectronic and nanoelectronics applications [20,24,27–29]. It has distinct optoelectronic properties, including an intrinsic bandgap [30,31], efficient photovoltaic (PV) response [32,33] and photoluminescence (PL) [34]. Monolayer of $MoSe_2$ display a direct bandgap (~1.55 eV) compared to their bulk counterparts, which show an indirect bandgap (~1.1 eV) [31]. It is a promising candidate for flexible nanoelectronic devices such as ultrathin PV systems [33], photodetectors [32], switchable transistors [34,35], and thermoelectric applications [27] due to its unusual optoelectronic properties and atomic-thickness. Moreover, an ultrathin nanosheet of $MoSe_2$ has a mobility of ~ 50 $cm^2 V^{-1}s^{-1}$ at ambient temperature [35], which nearly quadruples when the temperature is reduced to 78 K. Hence, $MoSe_2$ monolayer has appeared as a potential two-dimensional material for next generation ultrathin nanoelectronic applications.

Unlike the $MoSe_2$ monolayer (direct bandgap), the gallium nitride (GaN) monolayer is an indirect bandgap 2D material [21,36]. The mechanical and dynamic stabilities of GaN single layer have been revealed through elastic constants and phonon dispersion respectively [37]. The GaN monolayer indicates a high Poisson's ratio of 0.49 and a smaller in-plane stiffness of 103.60 N/m as compared to $MoSe_2$ monolayer mechanical response [38]. It is worth mentioning that the synthesis of GaN monolayer is achieved experimentally [39–41]. Monolayer of GaN has shown excellent lithium-ion storage capacity, according to recent experimental study. After 100/1000 cycles at 0.1/1.0 A g^{-1}, electrode based on GaN monolayer have a discharge capacity up to 702/600 mA h g^{-1} [42]. Since $MoSe_2$ and GaN monolayers are both 2D semiconductor materials, they have an almost identical structure and equivalent lattice parameters ($a_{GaN} = 3.20$ Å and $a_{MoSe2} = 3.22$ Å). Therefore, a 2D van der Waals heterostructure ($MoSe_2$/GaN) stacked by $MoSe_2$ and GaN monolayers is supposed to be a promising photocatalyst for solar energy conversion and overall water splitting. The current work demonstrates that the $MoSe_2$/GaN vdW heterostructure, based on first principles calculations, has high mechanical and dynamical stability. Additionally, it has larger kinetic over-potentials, suitable band edge positions and complete hole-electron separation along with higher coefficients of absorption in the visible spectrum, suggesting that it is an excellent applicant for solar energy conversion by photocatalytic overall water splitting.

2. Computational method

The ultrasoft pseudopotential (USPP) approach, used in the CASTEP, is adopted for all density functional theory (DFT) calculations [43]. The exchange–correlation (XC) function is controlled by using the Perdew Burke Ernzerhof (PBE) under the generalized gradient approximation (GGA) [44]. The vdW density functional corrections are considered to characterize the long-range van der Waals interactions by using the DFT-D2 approach of Grimme [45]. The vacuum space is set along the z direction to prevent the interaction between adjacent layers. The thickness of vacuum layer ~ 10 Å is normally considered enough to simulate the 2D limit. Here, in this calculation to obtain more accurate results the vacuum region is set to 20 Å. The Brillouin zone was sampled by adopting the Monkhorst pack mesh of $10 \times 10 \times 1$ with the cutoff energy of 500 eV for monolayers and heterojunctions structural relaxation and electronic properties. The total energy criterion convergence is set to 10^{-5} eV, and all of the structures are relaxed till each atom experience a force less than 0.01 eV/Å. The valence states for Mo, Se, Ga and N atoms were selected $4d^5\ 5\ s^1$, $3d^{10}\ 4\ s^2\ 4p^4$ and $3d^{10}\ 4\ s^2\ 4p^1$ and $2\ s^2\ 2p^3$ respectively. Moreover, it is a familiar fact that bandgap (E_g) of semiconductors is usually underestimated by GGA calculations and inaccurately interprets the conduction band characteristics. Thus, the correct values of energy bandgap are often calculated by Heyd-Scuseria-Ernzerh (HSE) and *GW* methods. Here, in present work, the electronic (band structure and DOS) and optical properties of isolated monolayers ($MoSe_2$, GaN) and heterojunctions ($MoSe_2$/GaN) are calculated using the hybrid functional (HSE06) method [46]. The electronic properties of heterostructures ($MoSe_2$/GaN) under various applied biaxial strain and external electric field are also studied using the HSE06 to acquire accurate trend.

The optical absorption coefficient $\alpha(\omega)$ can be calculated by implementing expression $\alpha(\omega) = \sqrt{2}\,\frac{\omega}{c}\left[\sqrt{\varepsilon'(\omega)^2 + \varepsilon''(\omega)^2} - \varepsilon'(\omega)\right]^{\frac{1}{2}}$, here $\varepsilon'(\omega)$ represents real and $\varepsilon''(\omega)$ represents imaginary components of the dielectric function $\varepsilon(\omega)$, whereas c represents the speed of light. The

Table 1
Geometry optimized lattice parameters (a), bonds length (d), interlayer distance between adjacent monolayers (h), formation energy (E_f), electronic bandgaps (E_g^{PBE} and E_g^{HSE06}), the kinetic over-potentials of OER (ΔE_v) and HER (ΔE_c) and the (ΔV) differences of vacuum levels at the two adjacent surfaces for three stacked (vertically) $MoSe_2$/GaN vdWHs.

Patterns	a (Å)	d_{Ga-N} (Å)	d_{Mo-Se1} (Å)	d_{Mo-Se2} (Å)	H (Å)	E_f (eV)	E_g^{PBE}(eV)	E_g^{HSE06}(eV)	ΔE_V	ΔE_C	ΔV
$MoSe_2$	3.269		2.513	2.513		−0.59	1.56	2.13	0.77	1.29	
GaN	3.215	1.856				−0.07	2.14	3.30	0.54	0.36	
AA	3.243	1.870	2.504	2.505	3.75	−0.27	1.37	2.16	0.39	0.51	6.21
AB	3.240	1.871	2.502	2.505	3.72	−0.21	1.62	2.15	0.40	0.51	6.34
BB	3.245	1.873	2.498	2.506	3.00	−0.31	1.61	1.97	0.33	0.44	7.19

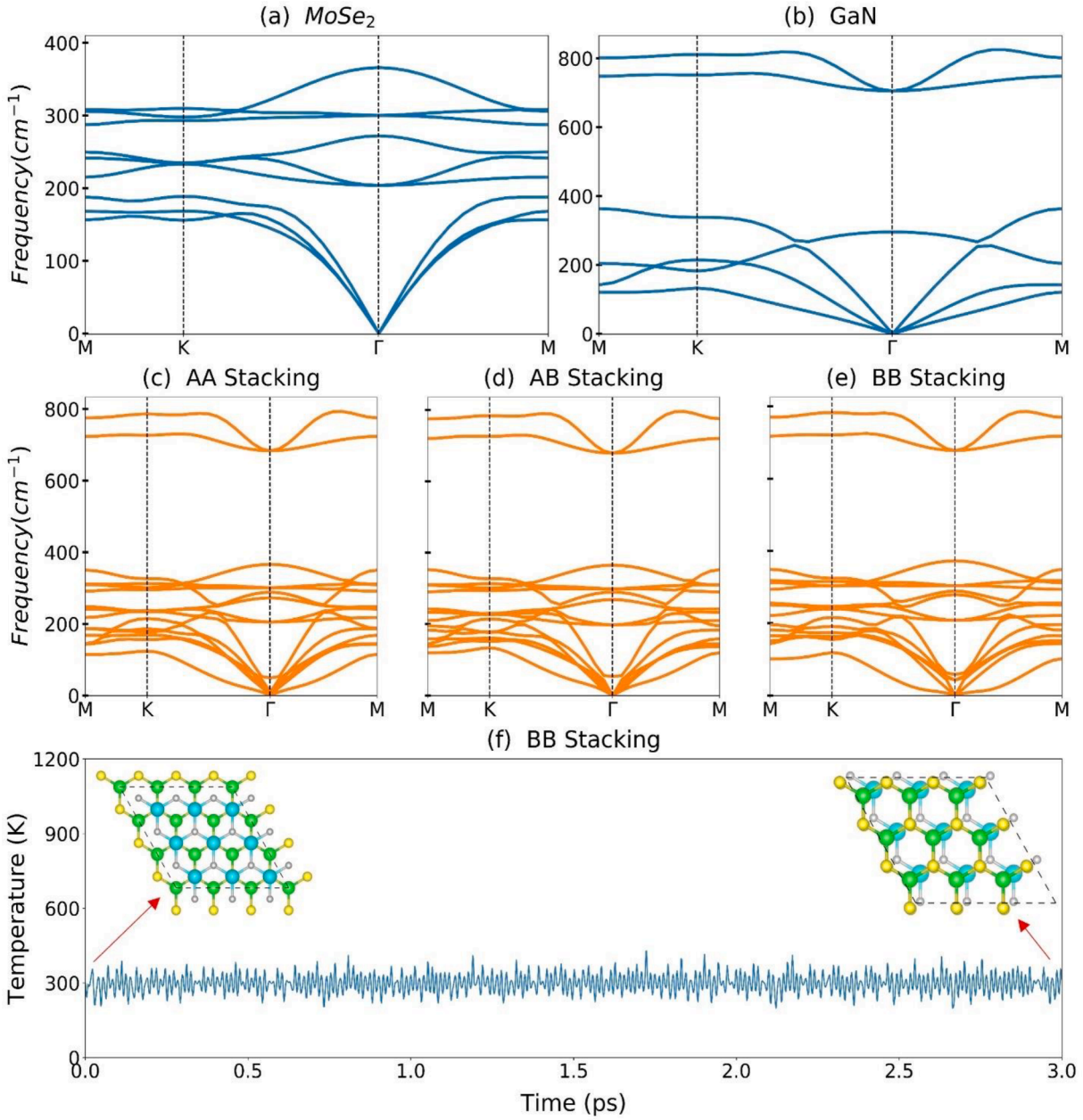

Fig. 2. Depicted the phonon spectrums of **(a)** $MoSe_2$ single layer, **(b)** GaN single layer, and three stacked $MoSe_2$/GaN vdWHs with stacking types of **(c)** AA, **(d)** AB and **(e)** BB. **(f)** molecular dynamics (MD) simulation at temperature of 300 K. Insets display $MoSe_2$/GaN vdWH crystal structure heat treatment (before and after).

absorption spectrum of $MoSe_2$/GaN vdW heterostructure ($MoSe_2$ and GaN monolayers) is measured on a dense k-point mesh of 24 × 24 × 1 to obtain the accurate optical spectra. The interatomic-force-constant matrix was used to calculate the phonon dispersion, which was collected at phonon wave vectors of *k*-point grid 9 × 9 × 1 from dynamical matrices by employing density functional perturbation theory (DFPT) performed with the Cambridge Serial Total Energy Package code along-with 2D open-boundary conditions [47].

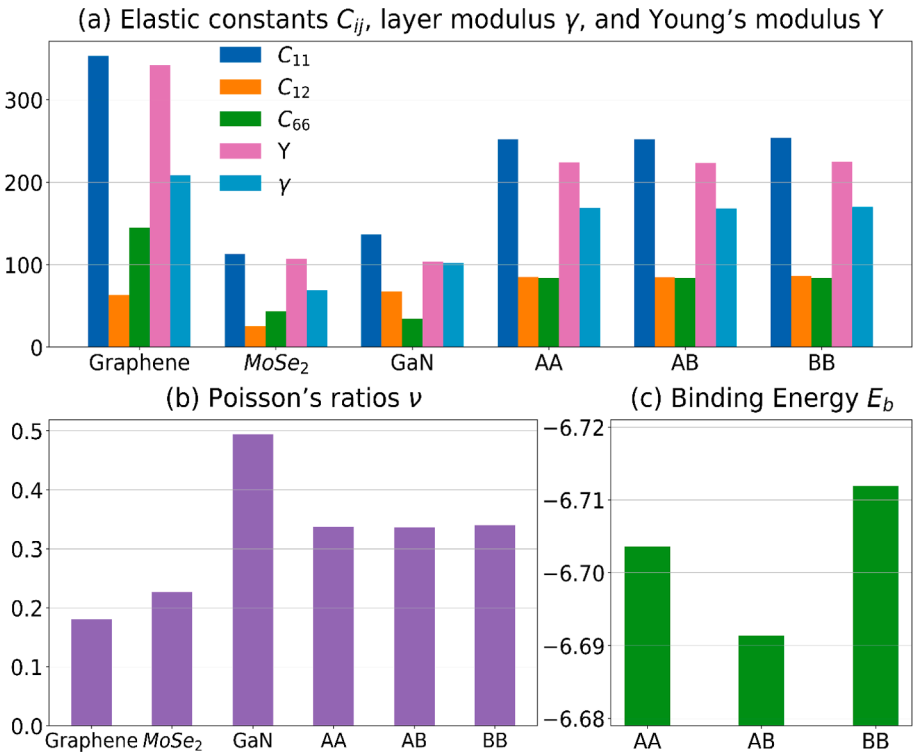

Fig. 3. Illustrated the **(a)** Elastic constants (C_{ij}), Young's modulus (Y), layer modulus (γ) **(b)** Poisson's ratios (ν) and **(c)** Binding energy (E_b).

3. Results and discussion

3.1. Geometric structure

There are three stacking configurations of $MoSe_2$/GaN vdW heterostructure are constructed, as seen in Fig. 1, denoted by the letters AA (any Ga atom is the center of rotational symmetry), AB (upper and lower layers are superimposed on each other), and BB (any Ga atom on top of Se atom). Among them, AA is the original model, and other models are obtained from the horizontal movement of the GaN monolayer in the original model. The geometry optimized lattice constants for the hexagonal $MoSe_2$ and GaN monolayers are 3.27 and 3.22 Å, which are well consistent with existing literature (3.30/ $MoSe_2$ and 3.25/GaN) [48–50]. The range of optional counterparts is limited by lattice matching criterion for constructing a heterostructure. The $MoSe_2$ and GaN monolayers have a lattice mismatch of less than 1.67 %, calculated by $\frac{a_{MoSe_2}-a_{GaN}}{a_{GaN}}$, suggesting that they can be easily stacked and build a preferred vdW heterojunctions. All the constructed heterostructures (AA, AB, BB) have almost the same lattice parameters, as the $MoSe_2$ and GaN monolayers, as seen in Table 1.

3.2. Stability analysis

The phonon dispersion of $MoSe_2$/GaN vdW heterostructures was calculated to assess their dynamical stability. The phonon spectrum of $MoSe_2$ and GaN monolayers were also studied for comparison. Fig. 2 is depicting the phonon dispersion of monolayers of $MoSe_2$, GaN and heterostructures of $MoSe_2$/GaN. Through the entire Brillouin zone, no imaginary frequencies exist, which indicate the dynamic stability of the monolayers and heterostructures. The findings of phonon dispersions of $MoSe_2$ and GaN monolayers are consistent with existing literature and previous calculations, which often comprise merely positive frequencies [37].

In contrast, as seen in Fig. 2(a, b), comparable to graphene [21], $MoSe_2$ and GaN monolayers have 9 and 6 phonon branches, containing transverse acoustic (TA) and in-plane transverse optical (TO) and longitudinal acoustic (LA); optical (ZO) and out-of-plane acoustic (ZA) phonons. It's worth noting that the acoustic modes (LA and TA) have linear dispersion, whereas ZA has perfectly quadratic dispersion, this is a common aspect of two dimensional (2D) materials. When $MoSe_2$ monolayer and GaN monolayer are stacked to build $MoSe_2$/GaN vdWHs, as presented in Fig. 2(c-e), the intralayer and interlayer modes of lattice vibrations in $MoSe_2$/GaN vdWHs could be seen. The lower branches of GaN monolayer and upper branches of $MoSe_2$ monolayer vibration modes are superimposed via intralayer modes, which are usually triggered by intralayer chemical bonds. However, in $MoSe_2$/GaN vdWHs, $MoSe_2$ monolayer display the quadratic dispersion for ZA and GaN monolayer displays a linear dispersion, suggesting that the $MoSe_2$/GaN vdWHs seems to be more stable than the $MoSe_2$ single layer and GaN single layer. Interlayer modes that primarily driven by interlayer var dan Waals (vdW) forces, the layer breathing (LB) and shear (S) modes, as a result of relative moment of $MoSe_2$ and GaN monolayers, can be observed below 100 cm^{-1} [51], they can be either parallel or perpendicular to their normal. Moreover, the interlayer interaction could be altering the ZA of $MoSe_2$/GaN vdW heterostructures and minimizing the vibration frequency of ZA of stacking AA, AB, BB. Since the interlayer distance in BB stacking is the lowest (Table 1) as a result, there would be a lot of interaction between the adjacent layers. The BB stacking has improved substantially as compared to the ZA of the $MoSe_2$ and GaN monolayers, as seen in Fig. 2e. On the other hand, the interlayer distance in AA stacking is the highest and the interlayer interaction would be weak. Additionally, Ab initio molecular dynamics (AIMD) simulations were also used to confirm the stability of the BB-$MoSe_2$/GaN vdWH (Fig. 2f). For 3 ps, AIMD simulations are performed employing the standard ensemble NVT at ambient temperature. It can be seen in Fig. 1s, BB stacking is more stable as compared to other stackings (AA and BB). It is found that the heterostructure atoms are marginally vibrated near its equilibrium positions in the snapshot of the heterostructure (see insets of Fig. 2f) after heat treatment, and no broken bonds and geometric reconstruction happened throughout the whole simulation phase, which confirms the thermal stability of the constructed $MoSe_2$/GaN vdW heterostructure, see the insets of Fig. 2f. We have also calculated Gibbs free

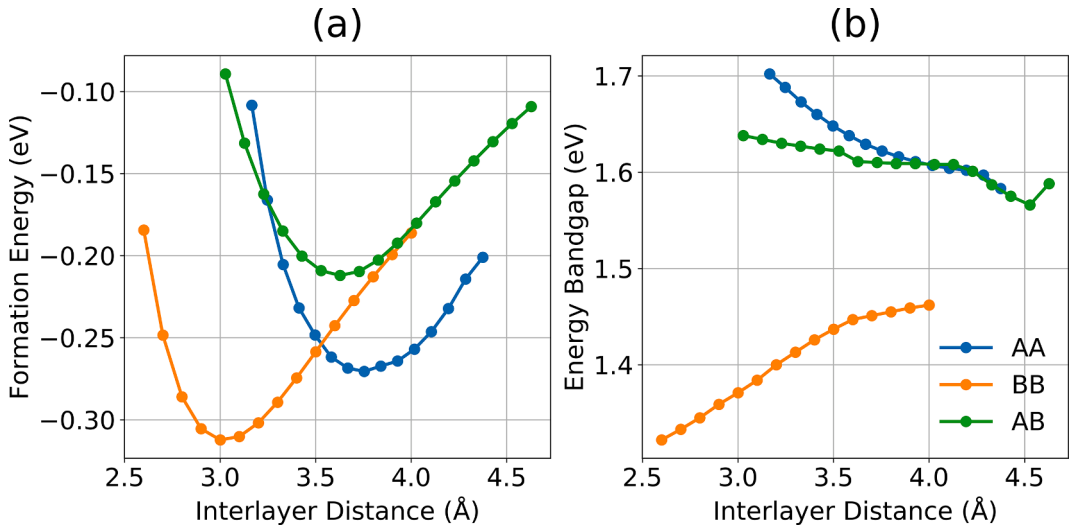

Fig. 4. Depicted the **(a)** The binding energies and **(b)** the curves of the bandgaps of AA(blue), AB(green) and BB(orange) stacking layers as a function of interlayer distance. (For interpretation of the references to colour in this figure legend, the reader is referred to the web version of this article.)

energy of all $MoSe_2$/GaN vdW heterostructures (Fig. 2s). It can be seen that BB stacking has more negative Gibbs free energy as compared to other stackings which show high stability.

The elastic constants of the $MoSe_2$/GaN vdW heterostructures were calculated to examine their mechanical stability. Elastic isotropy is exhibited by $MoSe_2$/GaN vdWHs due to the hexagonal symmetry, with independent C_{11}, C_{12}, and C_{66} elastic constants, and $C_{11} = C_{22}$. As depicted in Fig. 3a, criteria of mechanical stability ($C_{11} > C_{12}$, $C_{66} > 0$) is fulfilled by the elastic constants [52], indicating that all three vdWHs are stable mechanically. Whereas C_{11}, C_{12}, and C_{66} have following values 254.07, 86.39, 83.84 N/m respectively for BB stacking. $MoSe_2$ and GaN monolayers elastic constants along with graphene were also calculated for comparison, which are well consistent with previous findings [21,37,53]. The $MoSe_2$ monolayer Young's modulus (Y = 107.40 N/m) and poisson's ratio ($\nu = 0.23$) are comparable with existing density functional theory (DFT) based calculated findings (Y = 109.52 N/m and $\nu = 0.23$) [53]. Similarly, GaN single layer Poisson's ratio and Young's modulus ($\nu = 0.49$ and Y = 103.60 N/m) are well consisted with earlier outcomes ($\nu = 0.41$ and Y = 108.37 N/m) [37]. The Young's modulus (Y = 103.60 N/m) and poisson's ratio ($\nu = 0.49$) of graphene are also in good agreement with existing theoretical findings (Y = 335 N/m and $\nu = 0.16$) [21]. Furthermore, the larger C_{ij} of $MoSe_2$/GaN vdWHs suggests that they have superior in-plane bonding than the pristine monolayers of $MoSe_2$ and GaN. The current work reveals that the $MoSe_2$/GaN vdWHs are mechanically more stable than the pristine monolayers of $MoSe_2$ and GaN.

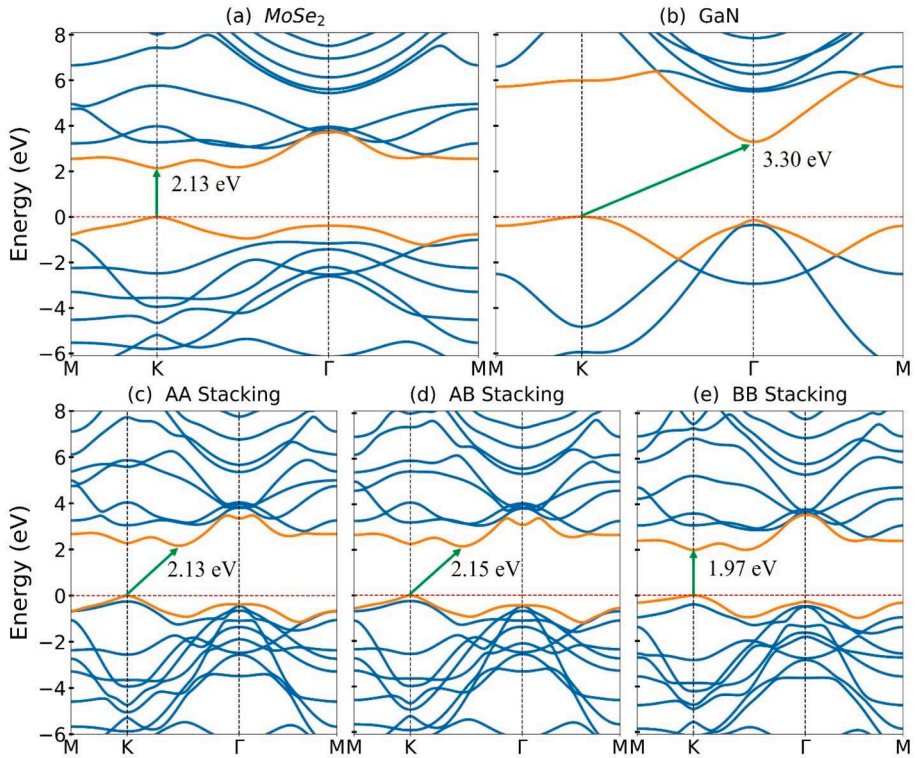

Fig. 5. *HSE06* band structures for **(a)** $MoSe_2$ single layer, **(b)** GaN single layer, and three stacked $MoSe_2$/GaN vdWHs with **(c)** AB, **(d)** AB, and **(e)** BB stackings.

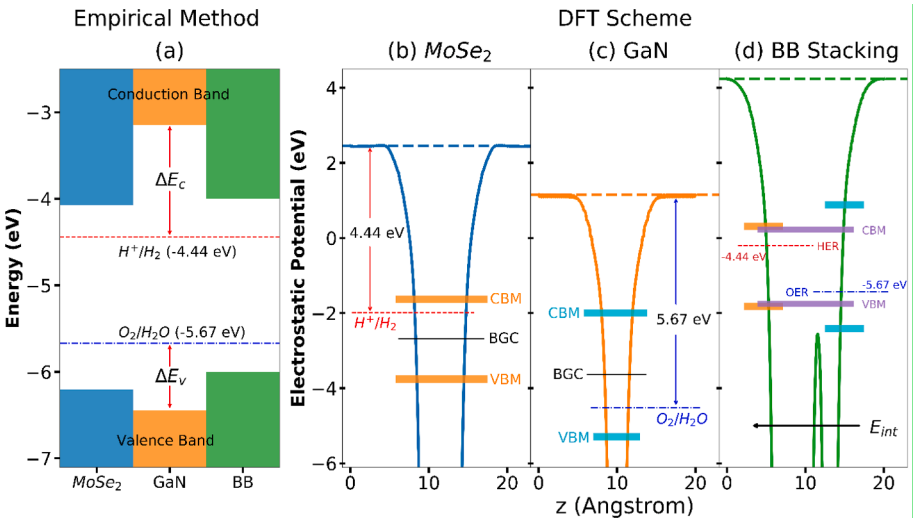

Fig. 6. Illustrated the estimated band-edges of $MoSe_2$ single layer, GaN single layer, and $MoSe_2$/GaN vdWH with BB stacking via **(a)** empirical scheme by setting the vacuum-level to zero and **(b-d)** DFT scheme where vacuum levels are depicted by dashed blue, orange and green lines for $MoSe_2$ monolayer, GaN monolayer and BB stacking respectively, and intrinsic electric field is denoted by E_{int} for the $MoSe_2$/GaN vdWH semiconductor material. (For interpretation of the references to colour in this figure legend, the reader is referred to the web version of this article.)

The binding energies of $MoSe_2$/GaN vdWHs were measured using $E_b = (E_T - E_{Mo} - E_{Se} - E_{Ga} - E_N)/N$, to evaluate the structural stability, where E_T and E_{Mo}, E_{Se}, E_{Ga}, E_N are the energies of the corresponding $MoSe_2$/GaN vdWHs and Mo, Se, Ga, N atoms respectively in their isolation states, whereas the total number of atoms in the $MoSe_2$/GaN vdWHs are represented by $N = 4$. Fig. 3c depicts the calculated binding energies. The BB heterostructure stacking has a sufficiently large binding energy of −6.712 eV/atom to stabilize the structure. Furthermore, all $MoSe_2$/GaN vdWHs have negative binding energy (E_b) values, indicating that their formations are all exothermic. It is worth to mention that the heterostructures' binding energies differed only slightly, showing that they may occur side by side.

To see whether the $MoSe_2$/GaN vdWHs can be facilely synthesized from $MoSe_2$ monolayer and GaN monolayer, further research is required. For that purpose, formation energies of all three stacking were determined by $E_f = (E_T - E_{MoSe2} - E_{GaN})$, where E_T, E_{MoSe2} and E_{GaN} are the energies of $MoSe_2$/GaN van der Waal heterostructures, $MoSe_2$ monolayer, and GaN monolayer. The computed results are described in Table 1. Due to their exothermicities, the formation energy values of all three stacking (AA, AB, BB) are negative, implying that they may be readily synthesized from $MoSe_2$ single layer and GaN single layer. It's important to note that the formation energies difference among all three stacked $MoSe_2$/GaN vdWHs are very minimal, suggesting that they can form simultaneously.

The variation of the interlayer-distance (d) is a well-established technique for tuning the electronic properties of vdW heterostructures. As per prior reports [54], the ultrathin $MoSe_2$ is an exceptionally strain sensitive 2D semiconductor material. Therefore, the orientation of $MoSe_2$ nanosheet is set to fix and the interlayer distance is controlled through changing the relative position of GaN monolayer, to prevent the interference from many other external factors. Fig. 4a shows the optimal outcome, in which the lowest E_f of −0.312 eV is obtained at d = 3.00 Å, which corresponds to BB stacking, the most robust vdW heterostructure with a bandgap of 1.37 eV (GGA). It should be noted that, the bandgap of $MoSe_2$/GaN heterostructure (BB) somehow increases linearly with the interlayer distance increment, which stems from the direct relationship between interlayer-distance and interlayer interaction. On the other hand, the trend of bandgaps in both AA and AB stackings shows an inverse correlation between the interlayer-distance and interlayer interaction (Fig. 4b).

3.3. Electronic properties

The hybrid functional (HSE06) electronic band structures of $MoSe_2$/GaN vdWHs are presented in Fig. 5. The HSE06 electronic band structure of $MoSe_2$ and GaN monolayers were also analyzed for comparison. The $MoSe_2$ monolayer is a 2D semiconductor with a direct bandgap at K-point, as seen in Fig. 5a. It shows a bandgap of 2.13 eV, in accordance with earlier findings (2.10 eV) [55]. On the other hand, the Gallium Nitride monolayer is a two-dimensional material with an indirect bandgap between K-point and Γ-point (Fig. 5b). The bandgap is estimated to be ~ 3.30 eV, which is well consisted with existing literature (~3.40 eV) [56]. The BB Stacking of $MoSe_2$/GaN vdWH exhibits a direct bandgap along the high symmetry K-point lines (Fig. 5e), While the AA and AB stackings demonstrated the indirect bandgap along K-point (VBM) and between K and Γ points (CBM) (Fig. 5(c, d)). It is important to note that direct-bandgap semiconductor materials are more significant for solar energy conversion applications because they absorb light more efficiently. The bandgaps of $MoSe_2$/GaN vdWHs are found to be connected to their stacked structural pattern. For instance, the PBE/HSE06 bandgaps are 1.62/2.13 eV, 1.61/2.15 eV, and 1.37/1.97 eV of the AA, AB, and BB stackings as seen in Table 1. Additionally, the density of sates (DoS) is also investigated to understand the participation of Mo, Se, Ga and N atoms in individual monolayers and participation of $MoSe_2$(GaN) monolayers in $MoSe_2$/GaN vdW heterostructures (Fig. 3s).

The band alignments of $MoSe_2$ monolayer, GaN monolayer and $MoSe_2$/GaN vdWH were determined by both an empirical formula and a DFT scheme to investigate the photochemical catalysis. In order to simplify the explanation, the most stable $MoSe_2$/GaN heterostructure among all three vdWHs, named as BB stacking, is considered in the discussion. Because the formation and binding energies of BB stacking are low as compared to other stackings (AA and AB). Moreover, the interlayer distance in BB stacking is lowest. Therefore, there would be a lot of interaction between the adjacent layers. The conduction band minimum and valence band maximum, through empirical formula, are calculated by using $E_{CBM/VBM} = -\chi \pm 0.5E_g^{HSE06}$ equations [57]. In this equation χ and E_g^{HSE06} denote the Mulliken electronegativity and bandgap. Where geometric mean is denoted by χ for the constituent atoms' Mulliken electronegativities. The calculated values of the χ are 5.14, 4.80 and 5.01 eV for $MoSe_2$ single layer, GaN single layer, and $MoSe_2$/GaN vdWH based on the Mulliken electronegativity values of Mo, Se, Ga and N atoms of 3.92, 5.89 eV, 7.30 and 3.20 respectively. The energy levels of $MoSe_2$/GaN vdWH with BB stacking, $MoSe_2$, GaN monolayers are presented in Fig. 6a, while AA and AB stackings are illustrated in Fig. 4s. The VBM(CBM) of $MoSe_2$ monolayer is higher than that of GaN monolayer, implying that the $MoSe_2$/GaN vdWH has a standard type-I band alignment. The energy difference between the water reduction potential and CBM is known as ΔE_C and between water oxidation potential and VBM is known as ΔE_V, as seen in Fig. 6a, are

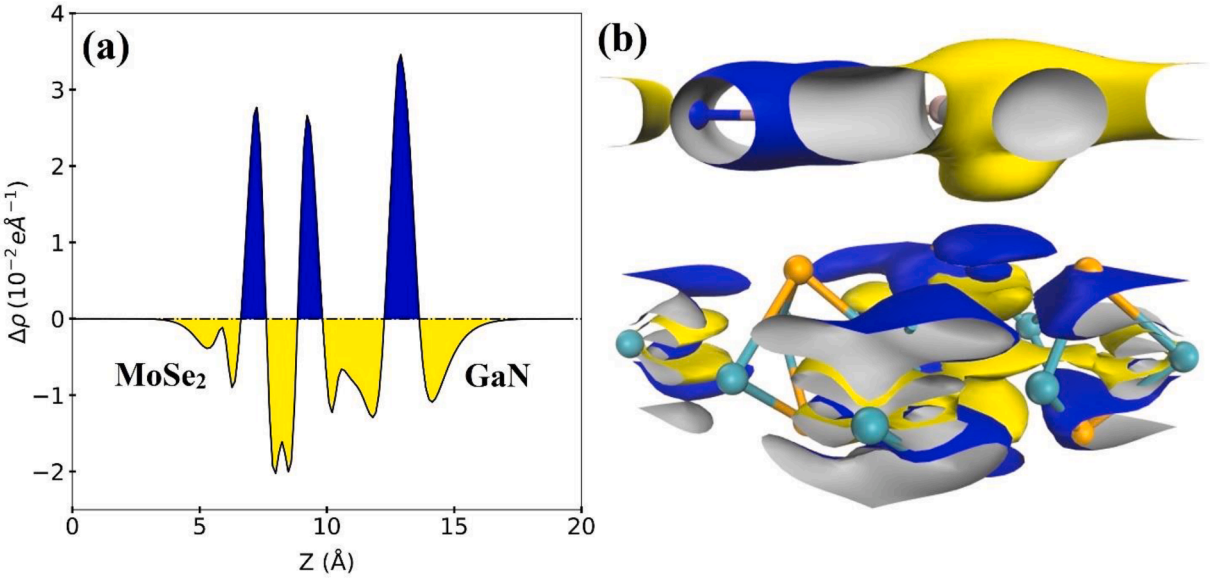

Fig. 7. Presented the plane-averaged **(a)** charge density difference (CDD) and **(b)** 3D plot of $MoSe_2$/GaN vdW heterostructure. The positive values (blue region) and negative values (yellow region) correspond to the charge accumulation and depletion. The heterojunction is constructed at isosurface value of 0.005 $eÅ^{-3}$. (For interpretation of the references to colour in this figure legend, the reader is referred to the web version of this article.)

referred to as kinetic over-potentials and are necessary to drive the redox reactions. It is observed that redox reactions are derived for all $MoSe_2$/GaN vdW heterostructures by adequately large-kinetic over-potentials. Hence, the position of band edges for all $MoSe_2$/GaN heterostructures (AA, AB, and BB stackings) fulfills the photocatalytic overall water-splitting requirement (Fig. 4s).

The density functional theory (DFT) is formally accurate to determine the bandgap center E_{BGC}() energy, according to a well-known theorem [58], while there are flaws in the exchange–correlation (XC) energy of the Kohn Sham DFT. Furthermore, since E_{BGC} is independent of the selection of XC functionals [59], Perdew-Burke-Ernzerhof (PBE) can be used to estimate the E_{BGC} at a smaller computational cost. The positions of band-edges (E_{VBM} and E_{CBM}) are calculated by the expressions: $E_{CBM/VBM} = E_{BGC} \pm 0.5E_g^{HSE06}$, whereas band-edges of $MoSe_2$/GaN vdWH with BB (AA and AB) are presented in Fig. 6d (Fig. 5s) by violet colors. The DFT scheme findings are well consisted with the empirical results when it comes to the positions of band edges. Additional details can also be obtained by using DFT scheme. It can be seen that there is only one vacuum level for an isolated $MoSe_2$ (GaN) monolayer in the absence of vertical electric-field. The reduction potential of H^+/H_2 and vacuum level of isolated $MoSe_2$ single layer are illustrated by a red and blue dotted line (Fig. 6b), respectively. While the oxidation potential and vacuum energy level of isolated GaN single layer are illustrated by blue and orange dotted line (Fig. 6c), respectively.

Electronegativity difference between $MoSe_2$ and GaN monolayers causes flow of electrons from GaN layer towards $MoSe_2$ layer when these layers are stacked together to form $MoSe_2$/GaN vdW heterostructures. The flow of the electron transfer will persist untill the Fermi levels (FL) of both $MoSe_2$ and GaN monolayers are perfectly aligned. A built-in electric field (E_{int}) is formed due the dipole moment. Consequently, as shown in Fig. 6d, vacuum energy level of $MoSe_2$/GaN vdW heterostructure is not site dependent. Comparison of the vacuum levels of MoS_2 and GaN monolayers determined the contribution of these layers to CBM and VBM. Blue bands display CBM and VBM for the GaN layer, orange bands show CBM and VBM of the $MoSe_2$ layer whereas vacuum energy level, HER and OER are represented by green, red and blue dotted lines (Fig. 6d). The $MoSe_2$/GaN vdW heterostructure possess a conventional type-I band alignment as $MoSe_2$ has VBM(CBM) higher than that of GaN VBM(CBM). In fact, layer resolved atom projected band structures (see Fig. 6s (a)) show that the $MoSe_2$ layer form the CBM, while both $MoSe_2$ and GaN layer form the VBM of the $MoSe_2$/GaN vdWH. Therefore, photogenerated holes and electrons accumulate on the surfaces of the $MoSe_2$ monolayer and GaN monolayer, respectively. Furthermore, intrinsic electric field E_{int}, which is directed from the GaN monolayer to $MoSe_2$ monolayer (Fig. 6d, black arrow), permits flow of extra holes to the GaN monolayer, while transfer of electrons to the $MoSe_2$ monolayer, inhibiting the photogenerated holes and electron recombination. Similarly, OER occurs on a GaN monolayer surface, and the hydrogen evolution reaction (HER) takes place on a $MoSe_2$ layer surface.

Alternatively, the electrochemical potentials relative to the vacuum level are used to estimate the redox potentials of hydrogen and oxygen. The redox potentials of O_2/ H_2O and H^+/H_2 between the $MoSe_2$ monolayer and GaN monolayer surfaces change as a result of the difference in their vacuum levels. The value of ΔE_c is 0.44 eV to generate H_2 on $MoSe_2$ monolayer surface, and value of ΔE_v is 0.33 eV to yield O_2 on GaN monolayer surface for BB stacking against the H^+/H_2 and O_2/ H_2O redox potentials. $MoSe_2$/GaN with BB stacking effectively separate the holes and electrons and also attains reasonable ΔE_v and ΔE_c due to large value of ΔV (Fig. 5s). The kinetic over-potentials (ΔE_v and ΔE_c) are generally proportional to the photocatalytic efficiency. The values of ΔE_c for the $MoSe_2$/GaN vdW heterostructures range between 0.44 and 0.51 eV, whereas the values of ΔE_v range between 0.33 and 0.40 eV (Table.1). These large values of kinetic over-potentials (ΔE_v and ΔE_c) imply that the $MoSe_2$/GaN vdWHs possess higher water oxidation ability than the renowned two-dimensional g-C_3N_4 photocatalyst [60]. Hence, it can be concluded that within the broad range of light spectrum (visible to UV), $MoSe_2$/GaN vdWHs could be a potential photocatalysts.

The planar-average charge-density differential (z) along the z-direction normal to the surface is investigated to obtain a clearer understanding of the electrical characteristics of $MoSe_2$/GaN vdWH. The following formula is used to determine $\Delta\rho(z)$.

$$\Delta\rho(z) = \rho_{vdWH}(z) - \rho_{MoSe_2}(z) - \rho_{GaN}(z) \quad (1)$$

where $\rho_{vdWH}(z)$, $\rho_{MoSe_2}(z)$ and $\rho_{GaN}(z)$ are the plane averaged charge densities of the $MoSe_2$/GaN vdWH, pristine $MoSe_2$ and GaN monolayers, respectively. Apparently, charge redistribution occurs in $MoSe_2$/GaN heterojunction by the generation of hole-rich and electron-rich regions (Fig. 7). Charge redistribution features like charge accumulation (blue

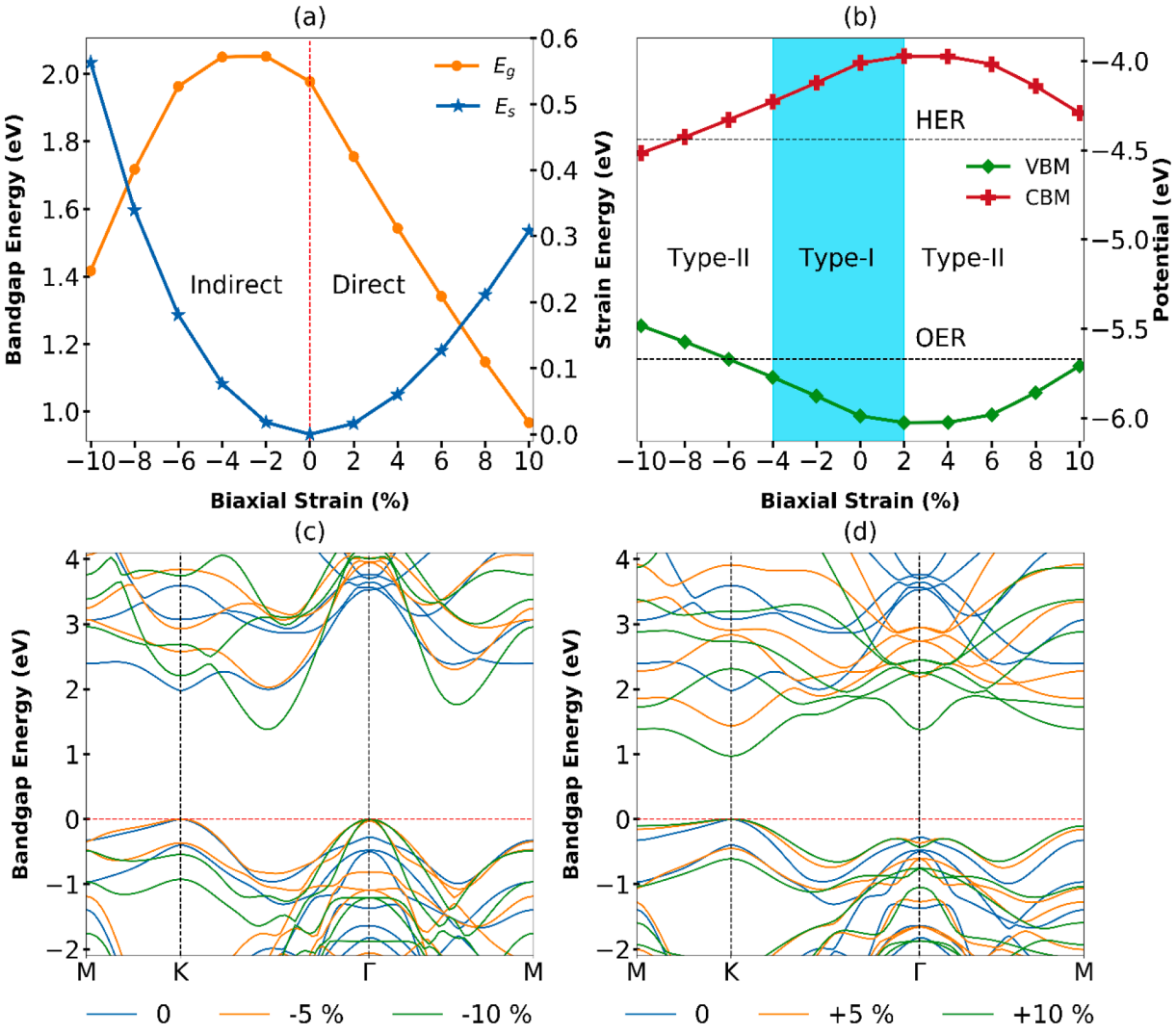

Fig. 8. Illustrated the biaxial strain effect on **(a)** strain energy (E_s) and bandgap (E_g), **(b)** position of VBM and CBM for water splitting and **(c, d)** electronic band structures.

isosurface) and charge depletion (yellow isosurface) are well recognized for causing electron polarization and the development of an interface dipole. In other words, negative values denote charge depletion whereas positive values indicate charge accumulation. Furthermore, the repulsion effect of surface charge is demonstrated by charge depletion, which readily induces surface orbital rehybridization. Current study suggests that the GaN layer provides electrons to the $MoSe_2$ layer in the interfacial region (Fig. 7). Consequently, electrons accumulate near the $MoSe_2$ monolayer whereas depletion of electrons occur in the GaN region. It could induce an intrinsic electric field (built-in) to appear with a path pointing from GaN to $MoSe_2$ layer, causing holes and electrons to drift in opposing directions and eventually achieving a balance with the diffusion force. Existing literature shows that vdW heterostructures have comparable charge redistribution characteristics [61].

3.4. Effect of strain on electronic properties

Previous studies have shown that under the influence of compressive or tensile strains, the electronic properties and band-edge positions can be tuned relative to water redox levels in vdW heterostructures [7,8]. Strain engineering is a facile and practical approach in the process of manufacturing 2D heterojunctions. In current work, different biaxial strains are employed to $MoSe_2$/GaN vdW heterostructure in form of compression and tensile. The hybrid functional (HSE06) is employed to achieve the correct results. The negative values ($\varepsilon < 0$) signify compressive strain, while the positive values ($\varepsilon > 0$) indicate tensile strain. The strain is described as $\varepsilon = (a - a_0)/a_0$ [62], where a_0 and a represent the unstrained and strained lattice parameters of heterostructure, respectively. Whereas strain energy is estimated by $E_s = (E_{strained} - E_{unstrained})/n$, where the total number of atoms in the unit-cell is denoted by n. Variation in bandgaps and strain energy under biaxial strain (from −10 % to + 10 %) is presented in Fig. 8a. The bandgap increases from + 10 % to −2% and decreases from −4% to −10 % under the effect of biaxial strain. It is found that the $MoSe_2$/GaN heterostructure has a direct bandgap for tensile strain and an indirect bandgap for compressive strain respectively. Therefore, it is interesting to utilize it in optoelectronic and photocatalysis systems as a direct and indirect semiconductor by applying strain. The obtained outcomes suggested that the shape of biaxial strain energy is an ideal-quadratic function (Fig. 8a), implying that $MoSe_2$/GaN with BB stacking is flexible [63]. Furthermore, within the elastic limit, all strains are reversible. As the lattice deformation is greatly affects the bandgap energy consequently it changes the position of VBM and CBM for water splitting under external strain (Fig. 8b). Considering that water splitting requires a hole potential above −4.44 eV and an electron potential under −5.67 eV, $MoSe_2$/GaN is appropriate for the water's decomposition in a broad range of strain from −4% to + 10 %. It is also observed that the tensile strain is more suitable for overall water splitting as compared to compressive strain.

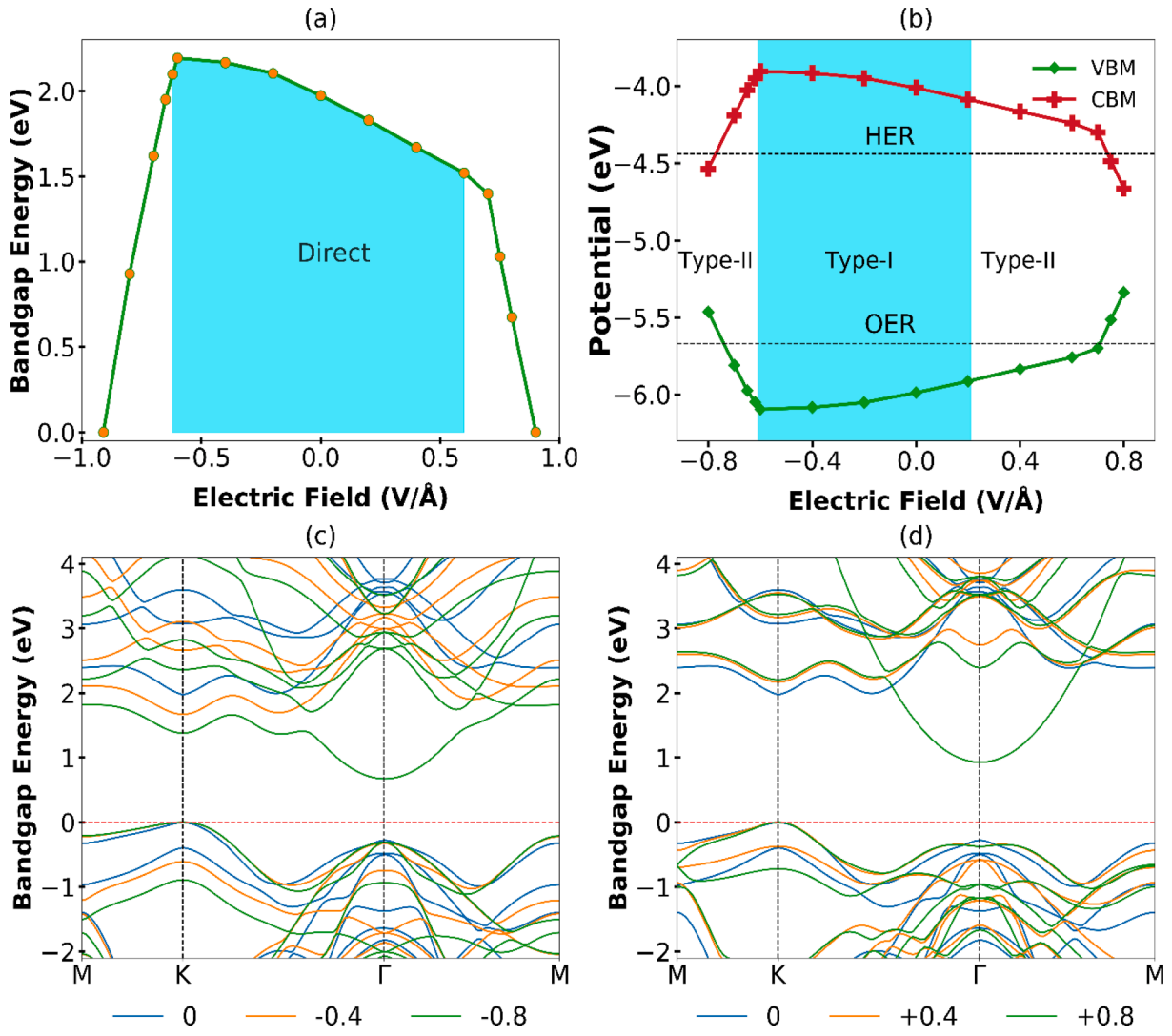

Fig. 9. Presented the external electric field effect on **(a)** bandgap (E_g), **(b)** position of VBM and CBM for water splitting and **(c, d)** electronic band structures.

Moreover, it can be observed in Fig. 8b that $MoSe_2$/GaN heterostructure is type-I and it can be used as type-II with little strain in semiconductor devices. It is obvious that direct bandgap type-II has an advantage over type-I vdW heterostructures [64]. The tensile strain is more beneficial as compared to compression strain due to direct bandgap. Additionally, by applying a slight strain it could act as a type-II heterostructure satisfying the overall water splitting conditions.

The band structures of $MoSe_2$/GaN heterostructure under compressive and tensile biaxial strains are displayed in Fig. 8(c, d). The increase of compressive strain shifted VBM from K to Γ, whereas the CBM dropped and moved in between K and Γ from K point leading to an indirect bandgap. It is also observed that the bands at K point are dropping and the bands at M point are getting higher until the strain reaches to −10 %. Firstly, compressive strain shows increasing behavior up to −2% and then shows the decreasing trend till −10 %. Contrary, tensile strain completely shows the decreasing trend. The increase of tensile strain has no effect on VBM, and it remains at K point, whereas the CBM dropped at K point which leads to a direct bandgap. When the compression and tensile strains finally reached to −10 % and + 10 %, the bandgaps were 1.42 and 0.97 eV respectively at HSE06 approximation. Moreover, the detailed projected band structure is also investigated under compressional (Fig. 6s) and tensile (Fig. 7s) strain of $MoSe_2$/GaN vdW heterostructure (BB stacking).

3.5. Electric field effect on electronic properties

Significant activities in materials science have been triggered with the application of an external electric field (E_{ext}), since it has the ability to modulate the electronic properties effectively, particularly in two dimensional (2D) materials [65–67]. Newly synthesized vdW heterostructures are expected to play significant roles by introducing an electric field in the diverse applications like energy storage and conversion systems, optoelectronics and photocatalytic water splitting. Thus, applying a parallel vertical electric-field to the direction of stacking is another approach to modulating the band-alignments of the $MoSe_2$/GaN heterojunction. This not only effects the band alignment, but also the vdW heterostructures characteristics which depend on the magnitude of the external electric-field. We analyzed the minor effect of electric-field (-0.9 to 0.9 eV/Å) on $MoSe_2$/GaN vdWH in current work. How the electronic properties (band structure) of $MoSe_2$/GaN are influenced by an electric field are illustrated in Fig. 9a. It is observed that the effect of positive electric field on bandgap shows decreasing trend up to 0.9 eV/Å. While the effect of negative electric field on bandgap first shows increasing then decreasing trend and approached zero at −0.9 eV/Å. It is found that $MoSe_2$/GaN heterostructure has direct bandgap from −0.40 to 0.60 eV/Å under influence of external electric field. Therefore, it could be a potential candidate for use in photocatalysis and optoelectronic devices as a direct and indirect semiconductor. As the

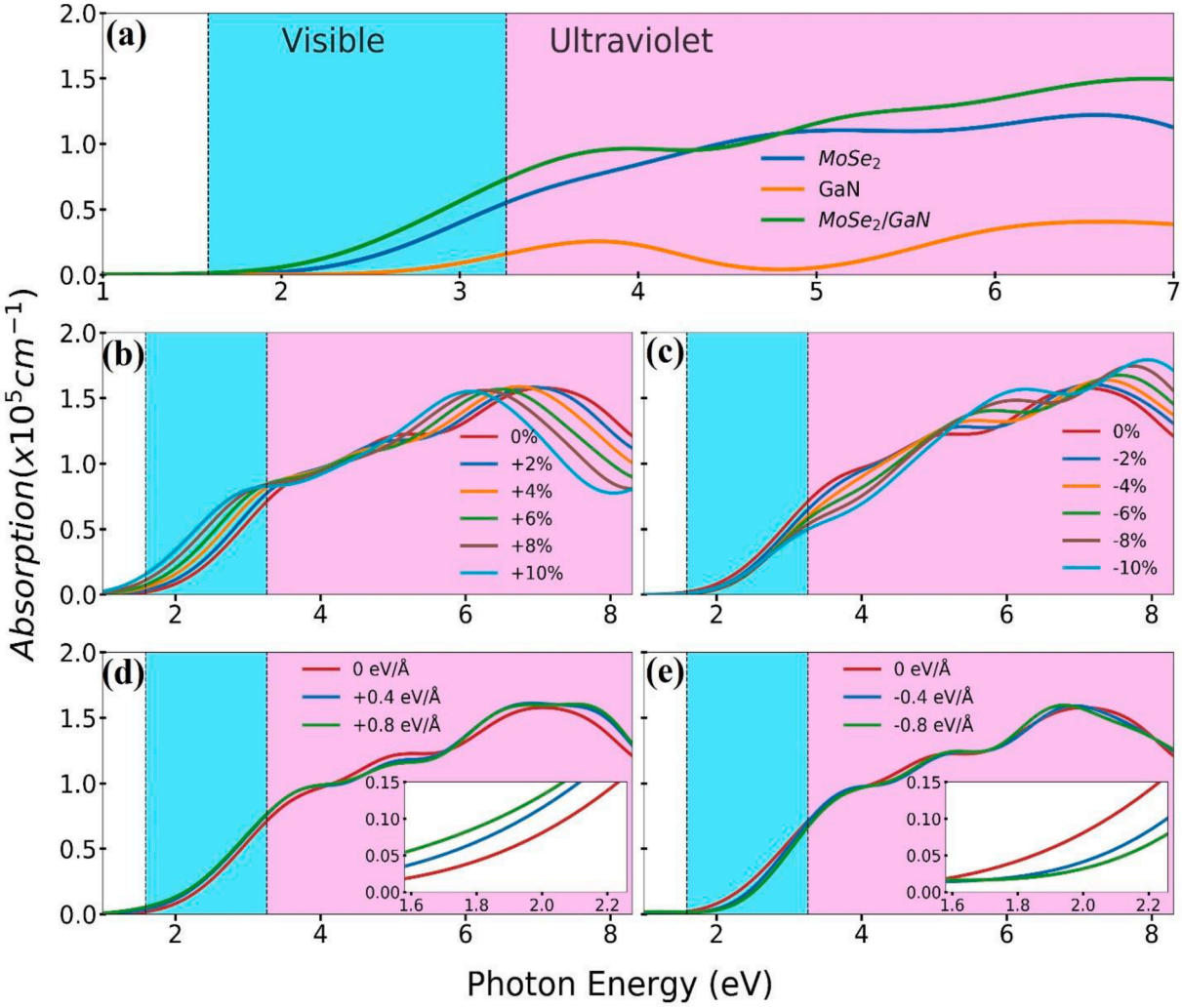

Fig. 10. Illustrated the optical absorption spectrum of monolayers of $MoSe_2$, GaN and $MoSe_2$/GaN vdW heterojunction **(a)** without strain and electric field (b) under compressional strain, **(c)** under tensile strain and **(d, e)** external electric field.

external electric field significantly affects the bandgap, it changes the position of CBM and VBM for water splitting under an electric field (Fig. 9b). Overall water splitting demands a hole potential less than −4.44 eV and an electron potential greater than −5.67 eV. Thus, $MoSe_2$/GaN is appropriate for the decomposition of water in broad electric field ranging from −0.7 to + 0.7 eV/Å. It is also noted that both negative and positive electric fields are appropriate for overall water splitting. It is worth mentioning that the $MoSe_2$/GaN interface can be used as a direct and an indirect bandgap type-II heterostructure by applying a minor external electric field.

The band structures of $MoSe_2$/GaN vdWH under negative and positive external electric field are presented in Fig. 9(c, d). The position of VBM is stable at K point in both positive and negative electric field. While the position of CBM is also located at K point within −0.40 to 0.60 eV/Å which leads to direct bandgap. On the contrary, under the effect of electric field beyond the −0.40 and 0.60 eV/Å, CBM shifted from K to Γ which leads to an indirect bandgap. The use of vertical electric fields is a great concept to control band alignments in vdWHs and improvement of orbital overlapping is intriguing. It opens the opportunity for carrier injection control between subsystems. This offers new opportunities for making field-effect transistors. It is essential to mention that the controlled type-II characteristics with hole-electron separation across the heterostructure interface make $MoSe_2$/GaN vdWH suitable for photovoltaic applications. Moreover, the detailed projected band structure of the $MoSe_2$/GaN vdW heterostructure (BB stacking) is also investigated under an external electric field (Fig. 8s).

3.6. Optical properties

The absorbing potential of a material in the visible spectrum of light plays a vital role in overall water splitting in photocatalysis. The $MoSe_2$ monolayer, GaN monolayer, and $MoSe_2$/GaN vdW heterostructure optical absorption responses are investigated and illustrated in Fig. 10. Both monolayers ($MoSe_2$ and GaN) and $MoSe_2$/GaN vdWH display excellent absorption intensities from the visible (10^4 cm^{-1}) to ultraviolet (10^5 cm^{-1}) region. The absorption of light by the vdW heterostructure begins in the visible area and rapidly rises with photon-energy, reaching a maximum absorption of 1.5×10^5 cm^{-1} at 6.9 eV (Fig. 10a). When compared to individual monolayers, the optical absorption intensity of the $MoSe_2$/GaN vdWH shows a significant improvement, indicating improved solar energy utilization. It could be interpreted by the fact that charge transfer and interlayer coupling encourage the overlapping of the orbital states in the heterobilayers.

Moreover, in this work, the effect of biaxial strain and external electric field on response of optical absorption of the $MoSe_2$/GaN vdWH has also been explored (Fig. 10(b-e)). It can be observed that the absorption of $MoSe_2$/GaN interface starts in the infrared region and shows intermediate peaks in the visible spectrum and achieves intense peaks in UV region. The mild absorption peaks are shifted towards a lower energy region (visible region) under the effect of tensile strains due to reduction

in the bandgap values (redshift). Similar trend can also be seen for intense peaks of absorption in the visible region (Fig. 10b). This observation is in excellent agreement with the existing literature of many two-dimensional heterostructure materials [62,68]. Surprisingly, under the impact of the applied compressional strain, the intensity of optical absorption for $MoSe_2$/GaN vdWH is considerably decreased, implying lower visible and greater UV light capture (Fig. 10c). The results of optical absorption reveal that $MoSe_2$/GaN heterostructure under tensile strain could be more suitable for visible region. As a result, under the influence of the applied biaxial strain, red or blue shifts in the optical-absorption spectrum are found. Additionally, we have also investigated optical absorption under the influence of external electric-field, as seen in Fig. 10(d, e). It can be seen clearly after applying a positive electric field that the absorption intensity slightly rises with photon energy in visible region (inset of Fig. 10d). On the contrary, a decreasing trend is noted under the negative electric in the visible region (inset of Fig. 10e). While the mix trend can be observed in UV region for both positive and negative electric field. Variations in the bandgap may alter the photon absorption energy threshold that causes electrons to transfer between heterobilayers under applied biaxial strain and electric field. This modification in bandgap energy allows the threshold of optical absorption edges to be changed [62].

4. Conclusion

Stacking of various two-dimensional (2D) layered materials to develop van der Waals heterostructures (vdWHs) has lately been considered an efficient approach for achieving the desired photocatalytic and optoelectronic properties. Here, we theoretically explored the $MoSe_2$/GaN vdW heterojunctions, which have three achievable stacking formations, stacked by $MoSe_2$ and GaN monolayers. The elastic constants, phonon dispersions, binding energies, bandgaps, band-edge positions, kinetic over potentials and coefficients of absorption (optical) for $MoSe_2$/GaN vdWHs were thoroughly inspected by using the first principles calculations using hybrid functional (HSE06). The $MoSe_2$/GaN vdW heterojunctions are mechanically and dynamically stable, according to the calculation of elastic constants, phonon dispersions, binding energy, and ab-initio molecular dynamics simulation. Furthermore, the $MoSe_2$/GaN vdWHs are more mechanically stable than either $MoSe_2$ or GaN monolayers by themselves. On the other hand, to accomplish the effective charge separation in photocatalytic, optoelectronic, photovoltaic devices, converting the vdWHs from type-I to type-II has special importance and interest. An intrinsic type-I band alignment with a direct bandgap is demonstrated, and the $MoSe_2$/GaN vdW heterostructures have adequately high kinetic over potentials which could easily drive the redox process based on empirical equations and DFT scheme prediction. Moreover, we anticipated that under moderate strains and external electric fields, type-I $MoSe_2$/GaN vdW heterostructures can be converted to type-II vdWHs, which are advantageous for effective charge separation. Photogenerated electrons and holes advance on the $MoSe_2$ and GaN layer surface respectively, because of electrostatic potential difference between them and the band alignment characteristics. Consequently, OER occurs on the GaN monolayer surface, while the HER takes place on the surface of $MoSe_2$ monolayer. The absorption of $MoSe_2$/GaN interface begins in IR region and shows intermediate peaks in the visible region and attains intense peaks in UV region along with high optical absorption coefficients, up to 10^5 cm^{-1}. Additionally, the mild absorption peaks are shifted towards lower and higher energy regions under tensile and compressive strains, respectively. No notable change is observed in optical absorption under external electric field. Recent work shows that the novel $MoSe_2$/GaN vdW heterostructures are potential applicants for photocatalytic overall water splitting when strain and external electric field is applied.

Declaration of Competing Interest

The authors declare that they have no known competing financial interests or personal relationships that could have appeared to influence the work reported in this paper.

Data availability

Data will be made available on request.

Acknowledgment

This work was supported by the National Key Research and Development Program of China (Grant No. 2018YFB2200500), the National Natural Science Foundation of China (Grant no. 61974170,61934007, 62050073), the Beijing Municipal Science and Technology Commission Project (Grant No. Z191100004819011), and the international collaboration project of Ministry of Science and Technology of China (Grant No. G2022184006L). F. K. Butt acknowledges the funding support from HEC through grant number 7435/Punjab/NRPU/R&D/HEC/2017. The author (Bakhtiar Ul Haq) extends his appreciation to the National Research Foundation of South Korea for supporting this work.

***Data** Availability*

All data generated or analyzed during this study are included in this published article and supplementary information file.

Appendix A. Supplementary material

Supplementary data to this article can be found online at https://doi.org/10.1016/j.mseb.2022.116195.

References

[1] A. Fujishima, K. Honda, Nature 238 (1972) 37–38.
[2] M. Rahman, C. Kwong, K. Davey, S. Qiao, W. Lee, M. Pasta, H. Yuan, G. Zheng, Y. Sun, Y. Li, Y. Cui, Nat. Nanotechnol 10 (2015) 980.
[3] J. Ran, G. Gao, F.-T. Li, T.-Y. Ma, A. Du, S.-Z. Qiao, Nat. Commun. 8 (2017) 1–10.
[4] H. Tong, S. Ouyang, Y. Bi, N. Umezawa, M. Oshikiri, J. Ye, Adv. Mater. 24 (2012) 229–251.
[5] X.L. Zheng, J.P. Song, T. Ling, Z.P. Hu, P.F. Yin, K. Davey, X.W. Du, S.Z. Qiao, Adv. Mater. 28 (2016) 4935–4942.
[6] K. Novoselov, A. Mishchenko, A. Carvalho, A.C. Neto, Science 353 (2016) aac9439.
[7] X. Zhang, Z. Meng, D. Rao, Y. Wang, Q. Shi, Y. Liu, H. Wu, K. Deng, H. Liu, R. Lu, Energ. Environ. Sci. 9 (2016) 841–849.
[8] Z. Guo, N. Miao, J. Zhou, B. Sa, Z. Sun, J. Mater. Chem. C 5 (2017) 978–984.
[9] D. Wang, Z. Zhang, B. Li, X. Duan, J. Semicond. 42 (2021), 092001.
[10] S. Wang, X. Wang, J.H. Warner, ACS Nano 9 (2015) 5246–5254.
[11] P. Chen, J. Shang, Y. Yang, R. Wang, X. Cheng, Appl. Surf. Sci. 419 (2017) 460–464.
[12] Y. Gong, J. Lin, X. Wang, G. Shi, S. Lei, Z. Lin, X. Zou, G. Ye, R. Vajtai, B. I. Yakobson, Nat. Mater. 13 (2014) 1135–1142.
[13] Z. Zhang, J. Huang, M. Zhang, Q. Yuan, B. Dong, Appl Catal B 163 (2015) 298–305.
[14] J. Su, G.D. Li, X.H. Li, J.S. Chen, Adv. Sci. 6 (2019) 1801702.
[15] Y. Fan, X. Ma, X. Liu, J. Wang, H. Ai, M. Zhao, J. Phys. Chem. C 122 (2018) 27803–27810.
[16] C. Li, J. Li, Y. Huang, J. Liu, M. Ma, K. Liu, C. Zhao, Z. Wang, S. Qu, L. Zhang, J. Semicond. 43 (2022), 021701.
[17] M.-L. Tsai, S.-H. Su, J.-K. Chang, D.-S. Tsai, C.-H. Chen, C.-I. Wu, L.-J. Li, L.-J. Chen, J.-H. He, ACS Nano 8 (2014) 8317–8322.
[18] Y. Liu, N.O. Weiss, X. Duan, H.-C. Cheng, Y. Huang, X. Duan, Nat. Rev. Mater. 1 (2016) 1–17.
[19] J. Wong, D. Jariwala, G. Tagliabue, K. Tat, A.R. Davoyan, M.C. Sherrott, H. A. Atwater, ACS Nano 11 (2017) 7230–7240.
[20] M. Chhowalla, H.S. Shin, G. Eda, L.-J. Li, K.P. Loh, H. Zhang, Nat. Chem. 5 (2013) 263.
[21] H. Şahin, S. Cahangirov, M. Topsakal, E. Bekaroglu, E. Akturk, R.T. Senger, S. Ciraci, Phys. Rev. B 80 (2009), 155453.
[22] K.S. Novoselov, A.K. Geim, S.V. Morozov, D. Jiang, Y. Zhang, S.V. Dubonos, I.V. Grigorieva, A.A. Firsov, science, 306 (2004) 666-669.
[23] R. Lv, J.A. Robinson, R.E. Schaak, D. Sun, Y. Sun, T.E. Mallouk, M. Terrones, Acc. Chem. Res. 48 (2015) 56–64.
[24] Q.H. Wang, K. Kalantar-Zadeh, A. Kis, J.N. Coleman, M.S. Strano, Nat. Nanotechnol. 7 (2012) 699.

[25] D. Kufer, G. Konstantatos, Nano Lett. 15 (2015) 7307–7313.
[26] A. Parmar, J. Kaur, M.D. Sharma, N. Goyal, J. Semicond. 42 (2021), 082001.
[27] Z. Yan, M. Yoon, S. Kumar, 2D Materials, 5 (2018) 031008.
[28] Y.-H. Lee, L. Yu, H. Wang, W. Fang, X. Ling, Y. Shi, C.-T. Lin, J.-K. Huang, M.-T. Chang, C.-S. Chang, Nano Lett. 13 (2013) 1852–1857.
[29] C. Ataca, H. Şahin, S. Ciraci, The Journal of Physical Chemistry C 116 (2012) 8983–8999.
[30] Y. Zhang, T.-R. Chang, B. Zhou, Y.-T. Cui, H. Yan, Z. Liu, F. Schmitt, J. Lee, R. Moore, Y. Chen, Nat. Nanotechnol. 9 (2014) 111.
[31] S. Tongay, J. Zhou, C. Ataca, K. Lo, T.S. Matthews, J. Li, J.C. Grossman, J. Wu, Nano Lett. 12 (2012) 5576–5580.
[32] Y.-H. Chang, W. Zhang, Y. Zhu, Y. Han, J. Pu, J.-K. Chang, W.-T. Hsu, J.-K. Huang, C.-L. Hsu, M.-H. Chiu, ACS Nano 8 (2014) 8582–8590.
[33] M. Bernardi, M. Palummo, J.C. Grossman, Nano Lett. 13 (2013) 3664–3670.
[34] M. Onga, Y. Zhang, R. Suzuki, Y. Iwasa, Appl. Phys. Lett. 108 (2016), 073107.
[35] S. Larentis, B. Fallahazad, E. Tutuc, Appl. Phys. Lett. 101 (2012), 223104.
[36] N. Sanders, D. Bayerl, G. Shi, K.A. Mengle, E. Kioupakis, Nano Lett. 17 (2017) 7345–7349.
[37] P. Lou, J.Y. Lee, ACS Appl. Mater. Interfaces 12 (2020) 14289–14297.
[38] Q. Peng, C. Liang, W. Ji, S. De, Appl. Phys. A 113 (2013) 483–490.
[39] W. Wang, Y. Li, Y. Zheng, X. Li, L. Huang, G. Li, Small 15 (2019) 1802995.
[40] T. Imaoka, T. Okada, S. Samukawa, K. Yamamoto, ACS Appl. Mater. Interfaces 9 (2017) 41629–41633.
[41] Z.Y. Al Balushi, K. Wang, R.K. Ghosh, R.A. Vilá, S.M. Eichfeld, J.D. Caldwell, X. Qin, Y.-C. Lin, P.A. DeSario, G. Stone, Nat. Mater. 15 (2016) 1166–1171.
[42] C. Sun, M. Yang, T. Wang, Y. Shao, Y. Wu, X. Hao, ACS Appl. Mater. Interfaces 9 (2017) 26631–26636.
[43] S.J. Clark, M.D. Segall, C.J. Pickard, P.J. Hasnip, M.I. Probert, K. Refson, M. C. Payne, Zeitschrift für Kristallographie-Crystalline Materials 220 (2005) 567–570.
[44] J.P. Perdew, K. Burke, M. Ernzerhof, Phys. Rev. Lett. 77 (1996) 3865.
[45] S. Grimme, J. Comput. Chem. 27 (2006) 1787–1799.
[46] J. Heyd, G.E. Scuseria, M. Ernzerhof, J. Chem. Phys. 118 (2003) 8207–8215.
[47] T. Sohier, M. Calandra, F. Mauri, Phys. Rev. B 96 (2017), 075448.
[48] B. Wang, X. Wang, P. Wang, T. Yang, H. Yuan, G. Wang, H. Chen, Nanomaterials 9 (2019) 1706.
[49] K. Ren, Y. Luo, S. Wang, J.-P. Chou, J. Yu, W. Tang, M. Sun, ACS Omega 4 (2019) 21689–21697.
[50] B. Wang, X. Wang, H. Yuan, T. Zhou, J. Chang, H. Chen, Int. J. Hydrogen Energy 45 (2020) 2785–2793.
[51] C.H. Lui, L.M. Malard, S. Kim, G. Lantz, F.E. Laverge, R. Saito, T.F. Heinz, Nano Lett. 12 (2012) 5539–5544.
[52] F. Mouhat, F.-X. Coudert, Phys. Rev. B 90 (2014), 224104.
[53] L. Dong, J. Lou, V.B. Shenoy, ACS Nano 11 (2017) 8242–8248.
[54] P.K. Dubey, N. Yogeswaran, F. Liu, A. Vilouras, B.K. Kaushik, R. Dahiya, IEEE Trans. Electron Devices 67 (2020) 2140–2146.
[55] H. Shu, Y. Wang, M. Sun, PCCP 21 (2019) 15760–15766.
[56] Z. Zhang, Q. Qian, B. Li, K.J. Chen, ACS Appl. Mater. Interfaces 10 (2018) 17419–17426.
[57] R.G. Pearson, The Journal of Organic Chemistry 54 (1989) 1423–1430.
[58] J.P. Perdew, M. Levy, Phys. Rev. Lett. 51 (1983) 1884.
[59] M.C. Toroker, D.K. Kanan, N. Alidoust, L.Y. Isseroff, P. Liao, E.A. Carter, PCCP 13 (2011) 16644–16654.
[60] X. Wang, K. Maeda, A. Thomas, K. Takanabe, G. Xin, J.M. Carlsson, K. Domen, M. Antonietti, Nat. Mater. 8 (2009) 76–80.
[61] Z. Zhang, Z. Xie, J. Liu, Y. Tian, Y. Zhang, X. Wei, T. Guo, L. Ni, J. Fan, Y. Weng, PCCP 22 (2020) 5873–5881.
[62] M.M. Obeid, A. Bafekry, S.U. Rehman, C.V. Nguyen, Appl. Surf. Sci. 534 (2020), 147607.
[63] H. Din, M. Idrees, G. Rehman, C.V. Nguyen, L.-Y. Gan, I. Ahmad, M. Maqbool, B. Amin, PCCP 20 (2018) 24168–24175.
[64] X. Cai, W. Chen, X. Jia, L. Zhang, Q. Wang, B. Wang, X. Yang, Y. Liu, Y. Jia, J. Mater. Chem. C 8 (2020) 12291–12301.
[65] Y. Wang, L. Wang, J. Xia, Z. Lai, G. Tian, X. Zhang, Z. Hou, X. Gao, W. Mi, C. Feng, Nat. Commun. 11 (2020) 1–8.
[66] B. Lin, A. Chaturvedi, J. Di, L. You, C. Lai, R. Duan, J. Zhou, B. Xu, Z. Chen, P. Song, Nano Energy 76 (2020), 104972.
[67] H. Zeng, R.S. Chen, G. Yao, Adv. Electron. Mater. 6 (2020) 1901024.
[68] K. Ren, S. Wang, Y. Luo, Y. Xu, M. Sun, J. Yu, W. Tang, RSC Adv. 9 (2019) 4816–4823.